Near-Surface and Bulk Dissolution Behavior of γ′ Precipitates in Nickel-Based VDM® Alloy 780 Studied with In-Situ Lab-Source and Synchrotron X-ray Diffraction

Frank Kümmel [1,*] , **Massimo Fritton** [1] , **Cecilia Solís** [1,2] , **Armin Kriele** [2] , **Andreas Stark** [3] and **Ralph Gilles** [1]

[1] Heinz Maier-Leibnitz Zentrum (MLZ), TU München, 85748 Garching, Germany; massimo.fritton@frm2.tum.de (M.F.); cecilia.solis@hereon.de (C.S.); ralph.gilles@frm2.tum.de (R.G.)

[2] German Engineering Materials Science Centre (GEMS) at Heinz Maier-Leibnitz Zentrum (MLZ), Helmholtz-Zentrum Hereon, 85748 Garching, Germany; armin.kriele@hereon.de

[3] Helmholtz-Zentrum Hereon, Institute of Materials Physics, 21502 Geesthacht, Germany; andreas.stark@hereon.de

* Correspondence: frank.kuemmel@frm2.tum.de

Abstract: The dissolution of nano-sized Ni3Al-based γ′ precipitates was investigated in the newly developed polycrystalline nickel-based VDM® Alloy 780 at the surface and in the bulk region with in-situ lab-source and synchrotron X-ray diffraction. These studies are important in obtaining a deeper understanding of the strengthening mechanism responsible for the stability and long service lives of such superalloys. We found that the dissolution behavior of the γ′ phase is very similar at the surface and in the bulk region, but small deviations were detected. The dissolution of γ′ starts at around 800 °C and no γ′ was found at temperatures exceeding 970 °C. As a result, the elements Al and Nb, which were bound in the γ′ phase, dissolved into the γ matrix and strongly increased the γ lattice parameter, as their atomic size is larger than the γ-forming elements Ni, Co, and Cr. However, this effect was suppressed in the surface area. A second matrix γ phase was detected at the same temperature range as that of the dissolution of the γ′ phase in the lab-source XRD measurements. The newly formed γ-2 phase had a smaller lattice parameter than that of the initial γ matrix. We propose that the γ-2 matrix phase is a result of high-temperature surface oxidation, which consumes, among other elements, Al and Nb and, therefore, leads to the smaller γ lattice parameter.

1. Introduction

Polycrystalline nickel-based superalloys are a unique material class that are used in hot sections of modern gas engines in a variety of load-bearing parts, from structural applications such as casings and guide vanes to highly stressed rotating disks. The requirements for materials in these parts are challenging. In addition to a good monotonic strength, the most important properties are superior creep resistance and low cycle fatigue behavior at operating temperatures. Furthermore, good formability is required, as these parts are typically forged [1–6].

The superior high-temperature mechanical strength of these alloys can largely be attributed to their characteristic two-phase microstructure. In these alloys, nano-sized intermetallic precipitates (γ′, Ni$_3$Al-based, L1$_2$) are distributed coherently within a matrix (γ, Ni-based, A1) [7,8]. Typically, the γ matrix is strengthened by refractory alloying elements, such as Cr, Co, W, and Mo. In addition, Al, Ti, Nb, and Ta are utilized to produce an optimized volume fraction of the γ′-precipitation phase. Because the precipitates are generally small (≈10 to 100 nm), a major source of strengthening in these alloys is

the coherency strain between the γ- and γ' phases [9]. However, for a variety of Ni-based superalloys, it is well known that the γ-γ' lattice misfit decreases with increasing temperature [9–11]. This is the result of the lower expansion coefficient of the γ' phase in comparison with the γ phase. Furthermore, the coherency strain also influences the coarsening behavior of the precipitates and thus the long-term stability of the microstructure and the mechanical strength of the material at elevated temperature [12–14]. In addition to the γ/γ'-microstructure, micro-sized high-temperature stable phases (δ, Ni_3Nb-based, DO_a or η, Ni_3Ti-based, DO_{24} or carbides, A1) are present in these alloys to impede grain growth during the forging process (δ or η) or as a by-product of the processing history (carbides) [15–17].

One major goal for the future development of Ni-based superalloys is to increase their operating temperatures, which will result in improved efficiency of the engine and, therefore, lower fuel burn with less CO_2 pollution. Among these polycrystalline nickel-based superalloys, alloy 718 is the most widely used Ni-based superalloy, due to its good mechanical properties and processing characteristics [7,18,19]. In 718-type Ni-based superalloys, the austenitic matrix is mainly strengthened by a body-centered tetragonal intermetallic phase (γ'', Ni_3Nb-based, $D0_{22}$). However, the service temperature of alloy 718 is limited to about 650 °C, due to the instability of the γ'' phase, which transforms into the δ phase, leading to a dramatic loss of its creep resistance.

In recent decades, many efforts have been made to develop new polycrystalline Ni-based alloys with operating temperatures above 650 °C, while retaining the good mechanical and processing characteristics of alloy 718 [20–22]. One very promising candidate is the new VDM® Alloy 780 [23,24]. The most important difference in this new alloy, as compared with alloy 718, is the altered chemical composition, where Fe is replaced by Co and there is a higher Al-content in combination with a lower Ti-content [24].

The microstructure of the VDM® Alloy 780 was previously intensively investigated by the authors by scanning electron microscopy (SEM) and high-resolution transmission electron microscopy (HRTEM), as well as neutron diffraction (ND) and small-angle neutron scattering (SANS) [25–28]. The microstructure consists of the γ-matrix, the γ'-hardening phase, and the δ-, η-, and Nb/Mo-based high-temperature-stable carbide phases (hereinafter denoted as NbC, for clarity). Preliminary XRD results show that the Ti-based nitride phases are also present, along with the carbide phases in some cases. The space group of the different carbide and nitride phases is identical. Therefore, these high-temperature phases cannot be distinguished by diffraction in the current experiments, especially because their fractions are quite small. The fraction of the different phases strongly depends on the underlying annealing treatments. In-situ ND studies at high temperatures have allowed an approximate determination of the solvus temperatures of the different phases ($\gamma'_{solvus} \approx 950$ °C, and $\delta/\eta_{solvus} \approx 1020$–1030 °C), as well as the study of the evolution of their lattice parameters with temperature. These neutron experiments give rise to bulk material information.

In the application, the microstructure, both in the bulk region and locally at the surface, are very important for a long service life of the component. On the one hand, the microstructure in the bulk region is responsible for sufficient load tolerance of the component to minimize plastic deformation under load, because the microstructure in this area makes up a large part of the component cross-section. On the other hand, typical failure criteria include crack initiation during fatigue or critical oxidation, both of which typically start at the surface of the material. These two failure mechanisms are strongly related to the phases that are present at the surface. The main focus of this study is the comparison of the dissolution behavior of the γ' phase in the surface and bulk regions in the temperature range from 25 °C to 1000 °C. Laboratory X-ray diffraction (XRD) experiments were used to measure the phases near the surface, because the mean penetration depth of X-rays generated by conventional lab sources is limited to a few micrometers in metals [10,29,30]. In contrast, high energy X-rays, which are available via synchrotron light sources, were used to study the microstructure in the bulk region, as they easily penetrate several mil-

limeters into highly absorbing materials. With the selected photon energy of 100 keV, it was possible to measure the cylindrical samples with a diameter of 5 mm in so-called Debye–Scherrer geometry.

2. Experimental Procedure

The XRD measurements were performed with a high-resolution X-ray powder diffractometer (Section 3.2 Malvern Panalytical Ltd., Malvern, UK), which was operated with a molybdenum anode ($\lambda_{k\alpha,1}$ = 0.70932 Å, $\lambda_{k\alpha,2}$ = 0.71361 Å, Kα2/Kα1 intensity ratio of 0.5; E_{Mo} = 17.4 keV) and a tube current/voltage of 40 mA/55 kV in θ–2θ geometry. The Kβ radiation was filtered with a 0.075 mm thick Zirconium sheet. The instrument was equipped with a 1D linear real-time multistrip detector (X'Celerator, Malvern Panalytical Ltd., Malvern, UK) with an efficiency of 30% for Mo Kα1 radiation and a pixel resolution of 0.002° in 2θ. The beam was limited to a 10 mm horizontal width and vertical beam divergence of 1/8°. Axial divergence was reduced by inserting Soller collimators with an opening of 0.04 rad at the incident and reflected beam path. The illuminated sample volume was around 0.25 mm^3 in this experimental arrangement. Data recording was conducted with a step size of 0.008° in a 2θ range of 10° to 42° and a counting time of 50 s per step. A total of three diffraction patterns were recorded at each temperature step. These individual patterns were totaled for quantitative analysis to obtain better measurement statistics. The heating was performed via a strip-heating chamber (HTK 16, Anton Paar GmbH, Graz, Austria). The heating chamber was connected with a turbomolecular vacuum pump and a He-gas inlet. The heating of the sample was performed with a Pt-heating filament, through which a high direct current was applied, and the temperature was measured at the bottom of this Pt-filament by a thermocouple. To avoid diffusion and chemical reactions of the Pt-filament and the sample, a 0.2 mm spacer made of polycrystalline CVD diamond with a high thermal conductivity was placed between them.

The plate-like samples (15 mm in length, 15 mm in width and 2 mm in height) were cut out of a 15 × 15 mm^2 sized bar, ground to a grit size of 6 μm, and polished with a 3 μm and 1 μm diamond suspension. Therefore, no oxides, which were produced during the processing and heat treatment of the bar, were present at the measuring surface. The thermal procedure during the X-ray experiment is shown in Figure 1. Before each measurement, a vacuum of approximately 10^{-5} mbar was applied, followed by flooding the chamber with high-purity He gas (purity 99.999%). This procedure was repeated three times. During the experiments, a constant He flow was applied to reduce the oxygen content and to prevent oxidation of the samples as much as possible. After these presteps, the samples were heated to the measuring temperature at a rate of 100 °C/min, followed by maintaining the temperature for 15 min for thermodynamical stabilization. To compensate for thermal expansion of the samples and the heating filament, the height and tilting angle of the samples were properly aligned before recording the diffraction pattern. The total measuring time at each temperature was 80 min. After the three diffractograms, the samples were heated to the next temperature and measurements with identical set parameters were performed.

For the temperature calibration, XRD measurements were carried out on pure Ni (99.00%) and Pt (99.95%) sheets with thicknesses of 1 mm at 25 °C, 400 °C, 800 °C, 1000 °C, and 1200 °C. The range of the 2θ diffraction angles was chosen so that at least three individual diffraction peaks—(111), (020)] (022) for Ni and (111), (020), (022), and (311) for Pt—were covered, as they were necessary to get reliable lattice parameters. With these data, the actual sample temperature was calculated. The evolution of the temperature difference was very similar in both materials. The measured temperature of the filament was very similar to the calculated temperature of the sample surface, up to 800 °C. At 1000 °C, the temperature of the filament differed by 10 °C from the temperature of the sample surface.
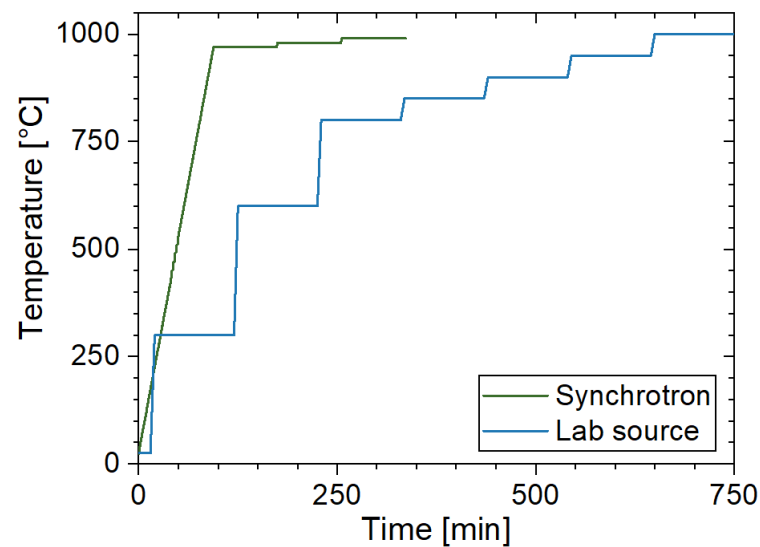
Figure 1. Schematics illustrating the heating process performed during the lab-source and synchrotron X-ray diffraction experiments.

Synchrotron X-ray diffraction patterns were obtained at the HEMS beamline [31] at PETRA III at DESY using a photon energy of 100 keV, which corresponds to a wavelength of 0.124 Å, resulting in a penetration depth of a few millimeters. The heating was performed using a modified Bähr DIL 805 A/D dilatometer. Cylindrical samples with a diameter of 5 mm and a length of 10 mm were used. The samples were cut out of the center of the same bar, from which the samples for the lab-source experiments were taken. The spot size of the X-ray beam on the sample was 1 mm^2, resulting in an illuminated sample volume of approximately 5 mm^3. An image detector (XRD1621, PerkinElmer Inc., Waltham, MA, USA) with a pixel size of 200×200 µm^2 and a resolution of 2048×2048 pixels was used to record the XRD patterns. The detector was positioned with a sample-to-detector distance of 1630 mm and the primary beam hit the detector center, allowing the complete recording of the Debye–Scherrer rings. The 2D patterns from the synchrotron measurements were treated with the software Fit2D [32]. It was possible to continuously heat the sample at a rate of 10 °C/min to a temperature of 970 °C. The measuring chamber was flooded with Ar during the experiments to reduce oxidation. Starting from this temperature, several isothermal segments with a holding time of 80 min were added until the temperature reached 990 °C, to enable measurement of the time-dependent dissolution of the γ'-phase and the high-temperature stable δ- and η-phases. The 2D patterns were recorded with a fast acquisition time of 4 s in the synchrotron experiments. Due to the large differences in acquisition times for the synchrotron and lab-source diffractograms, the temperature ramps differed strongly in the experiments. This difference will be discussed in greater detail in Section 4. The schematics illustrating the heating process performed during the synchrotron diffraction experiments is shown in Figure 1.

Rietveld refinements of the diffraction pattern were performed to obtain both the lattice parameters and the weight fractions of the present phases via Fullprof software [33], which was used in combination with GetControl software. The lattice misfit δ between the γ-matrix and the γ'-hardening phase was defined as the relative difference between the lattice parameters of the γ'-precipitates and the γ-matrix, according to the following formula:

$$\delta = \frac{2\left(a_{\gamma'} - a_{\gamma}\right)}{a_{\gamma'} + a_{\gamma}} \tag{1}$$

The peaks of the diffraction patterns were fitted with a Tompson–Cox–Hastings pseudo-Voigt profile function [34]. The instrumental peak-broadening of the lab-source and synchrotron diffractometer was evaluated by measuring a LaB$_6$ reference sample

(NIST-660C), with the same instrumental setup as that used for the VDM® Alloy 780 measurements. The LaB6 pattern were analyzed with a Pawley Fit to get the peak width (u, v, w, IG, y) and the asymmetry parameter (s/l and d/l).

The chemical composition of the investigated Ni-based VDM® Alloy 780 is shown in Table 1. VDM® Alloy 780 samples were investigated after a heat treatment resulting in a nearly full-age-treated microstructure that was mainly composed of γ and γ' (900 °C/11 h/air-cooled, 955 °C/1 h/furnace-cooled with 4 °C/min to 800 °C/8 h/furnace-cooled with 50 °C/h to 650 °C/8 h/air-cooled). The chemical composition of the γ and γ' phases in VDM® Alloy 780 was determined by atom-probe tomography in samples with a similar microstructure and processing history as that observed in a previously published article [35], Table 2. These compositions were used as the starting point to determine the scattering factors, which were necessary to calculate the volume fraction for the individual phases. Based on the previously published article [35], it was known that the chemical composition of the matrix and the precipitates changed during the precipitation/dissolution process. This change was compensated for by adjusted data refinement in the present work.

Table 1. Chemical composition of the investigated VDM® Alloy 780 samples measured by spark spectrometry.

Element	Co	Cr	Nb	Mo	Al	Fe	Ti	Ni
at.%	23.9	19.7	3.4	1.7	4.7	0.6	0.4	45.8

Table 2. Chemical composition of the γ and γ' phases in VDM® Alloy 780 samples measured by atom-probe tomography. Data from [35].
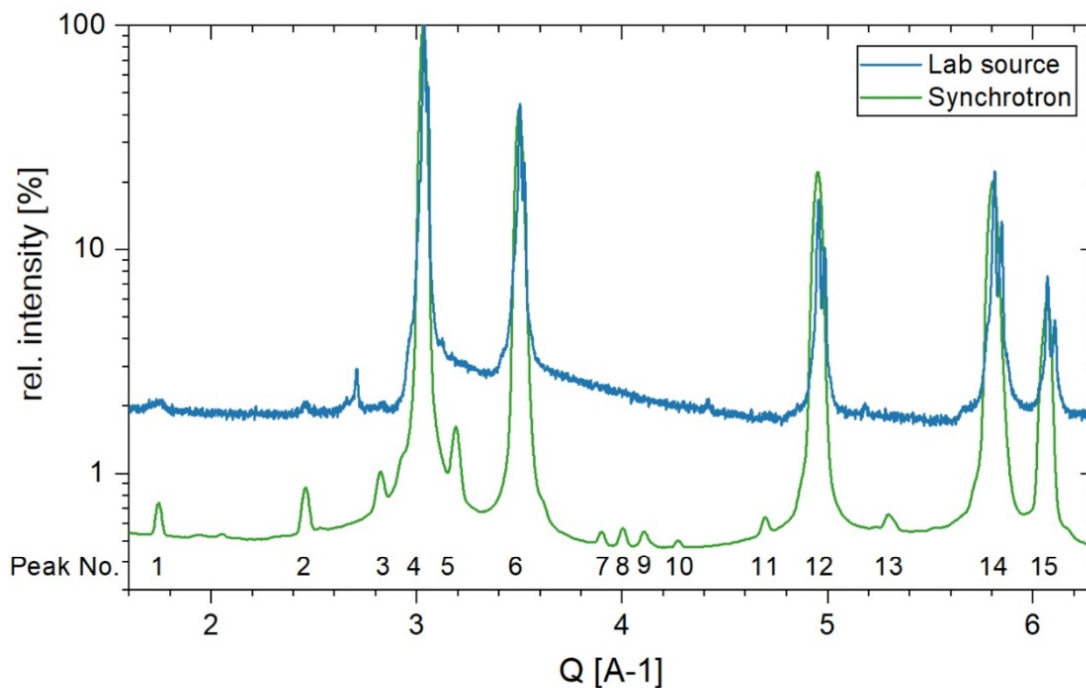
	APT Composition (at.%)							
Phase	**Co**	**Cr**	**Nb**	**Mo**	**Al**	**Fe**	**Ti**	**Ni**
γ	31.2	28.2	1.4	0.9	0.1	1.1	2.4	34.7
γ'	9.9	3.4	6.9	0.9	13.1	0.0	0.8	64.3

3. Results

3.1. Lattice Parameters and Weight Fractions at Room Temperature

In this section, the diffraction patterns at room temperature and their Rietveld refinements with the observed phases in the VDM® Alloy 780 are presented for both diffraction methods. In the diffractograms, the measured intensity I is plotted in contrast with the magnitude of the scattering vector Q. The magnitude of the scattering vector Q is defined as $Q = 4\pi \sin(\theta)/\lambda$, where θ is the scattering angle and λ is the incident wavelength. The I/Q diagram is used in this article instead of the oft-used I/2θ diagram, because the Q value normalizes $\sin(\theta)$ by the wavelength. Therefore, diffraction peaks that derive from experiments with different wavelengths (lab and synchrotron source) are at the same position of the *x*-axis.

The diffraction pattern at room temperature for the lab-source and synchrotron experiments are shown in Figure 2. In this graph, the intensity is normalized to the maximum measured intensity of the (111) γ peak of each diffraction method and a log10 scale is used for better comparability of the results. The ratio of peak intensity/background was significantly higher for the synchrotron measurements. As a result, the individual peaks for the minor phases (NbC, δ, and η) and for the isolated γ'-peaks were much more visible in this measurement. In total, 15 diffraction peaks were detected and analyzed from the synchrotron data. Many of those peaks overlapped with diffraction peaks from different phases, as shown at the right of Figure 2.

Peak No.	1	2	3	4	5	6	7	8
Reflex 1	100	111	201	111	211	200	210	220
	γ'	NbC	δ	γ'	δ	γ'	γ'	NbC
Reflex 2		110	200	111	202	200		
		γ'	NbC	γ	η	γ		

Peak No.	9	10	11	12	13	14	15
Reflex 1	003	211	311	220	411	311	222
	δ	γ'	NbC	γ'	δ	γ'	γ'
Reflex 2	204			220	206	311	222
	η			γ	η	γ	γ

Figure 2. Room temperature diffraction pattern measured with lab-source and synchrotron X-rays. On the bottom, a list of selected indexed diffraction peaks for the different phases is shown.

The simulated patterns and the difference plots for the whole measuring range are shown in Figure 3a,c for the lab-source and synchrotron measurements, respectively. In Figure 3b,d, a detailed view of the (311) diffraction peak (No. 14) is presented to illustrate the refinement of the strongly overlapping phases. The results from the lab-source X-ray diffraction could not be refined satisfactorily by taking into account only the two phases of γ and γ', as minor peaks at the right shoulder of the γ phase were not simulated. Therefore, a second γ phase (γ-2) with a significantly smaller lattice parameter (closer to the lattice parameter of pure Ni, a_{Ni} = 3,5239 Å [36]) was used to describe the measured peak shape in the lab-sourced XRD measurements. The origin of this phase will be discussed in Section 3.2. This γ-2 phase was not detected in the synchrotron RT measurements.

The calculated γ' weight fraction was in good agreement for both measurements, as shown in the tables in the insets of Figure 3a,c. Furthermore, the values in this work were in good accordance with previous ND results, which were performed with the high-resolution powder diffractometer SPODI [37–39] at MLZ, where a γ' weight fraction of 35% was found for samples with the same heat treatment [25]. However, a larger amount of the high-temperature phase (4.5 wt.% of δ and/or η) was measured in these ND results [25].

This difference between the synchrotron results and the ND results was probably due to the 200 times more highly analyzed sample volume of 1.000 mm^3 in ND. Therefore, the possibility of detecting the high-temperature phase, which is composed of micrometer-sized precipitates that are rather inhomogeneously distributed in the material, was much higher for ND.
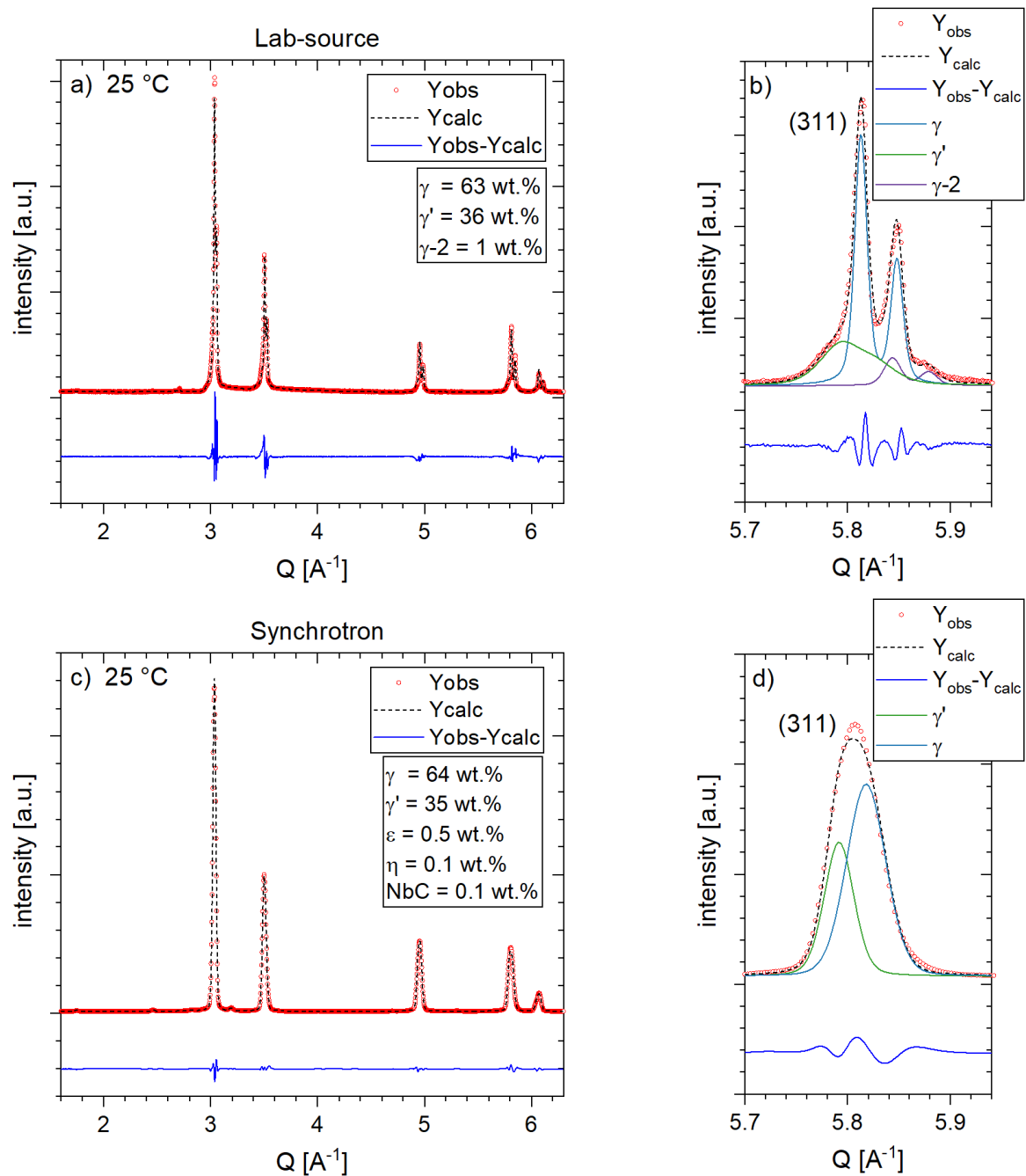

Figure 3. Rietveld refinement of the VDM® Alloy 780 samples tested at room temperature, with observed data (red circles), calculated data (black line), and difference plot (blue line), together with the position of the Bragg reflections of γ and γ′ for (**a**) the XRD and (**c**) the synchrotron measurements. A detailed view of the refinement of the (311) diffraction peaks is shown for the XRD- and synchrotron measurements in (**b**,**d**). In these diffractograms, the simulated patterns for the γ, γ′ and, if present, γ-2 phases are also shown.

3.2. Evolution of Lattice Parameters and Weight Fractions of the γ- and γ'-Phases at Elevated Temperatures

In total, five γ, γ', and γ-2 overlapping diffraction peaks were measured at each temperature to calculate precise lattice constants and weight fractions of the individual phases by a Rietveld refinement: (111), (200), (220), (311), and (222). In the synchrotron experiments, the (100), (110), (210), and (211) superlattice reflections of the γ' phase were also taken into account. In Figure 4a, the diffraction pattern of the (200) and (311) peaks are exemplarily depicted for the VDM® Alloy 780 sample at temperatures between 25 °C and 1000 °C for the lab-source X-ray diffraction experiments. The peaks were continuously shifted to lower Q-values with increasing temperatures, caused by the thermal expansion of lattice parameters. Furthermore, the shape and height of the peaks changed. This was related to a change in the fraction of the individual phases and their sizes and strains. In Figure 4b, an excerpt of the Rietveld refinement at 1000 °C of the (311) peak is depicted. No γ' phase was present at this temperature, while the peak of the γ-2 phase was very pronounced. Both peaks were very narrow, which meant that no significant strain- or size-broadening was present at this temperature.
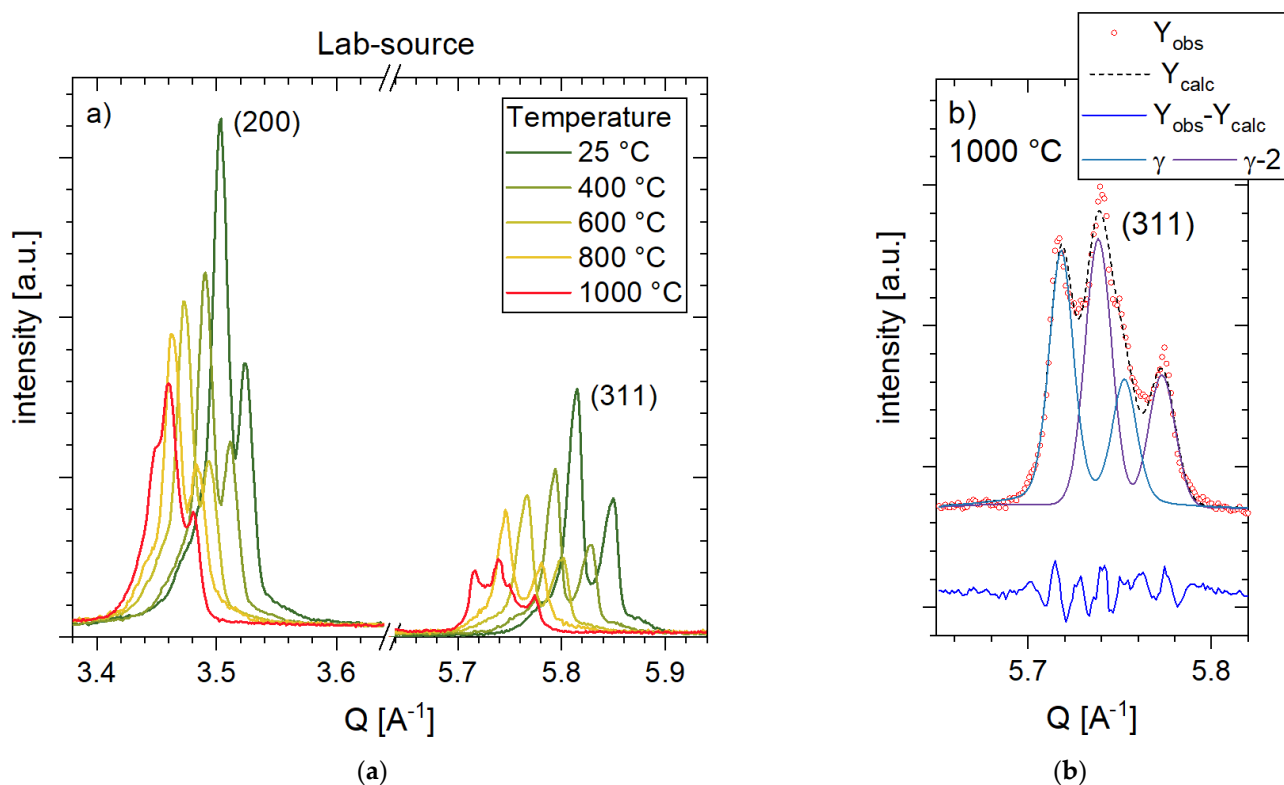

Figure 4. (**a**) Lab-source X-ray diffraction pattern of VDM® Alloy 780 tested at different temperatures (25 °C to 1000 °C). In (**b**), a detailed view of Rietveld refinement at 1000 °C of the (311) diffraction peaks is provided: observed data (red circles), calculated data (black line), and difference plot (blue line). In this diffractogram, the simulated pattern for the γ and γ-2 phases is also shown.

The evolution of the synchrotron diffraction pattern is depicted in Figure 5 in the temperature range from 710 °C to 970 °C. In these diffractograms, the dissolution of the isolated (100), (210), and (211) γ' peaks is shown with increasing temperature. As the (100) peak showed the highest intensity of the isolated γ' peaks, the evolution of the γ' phase amount was followed by this peak. The height of these peaks remained constant up to a temperature of 750 °C. Above this temperature, the peak height continuously decreased, which indicated a dissolving of the phase. The peaks fully disappeared within 60 s during the first holding segment, at 970 °C. In contrast, the peaks of the high-temperature δ- and η-phases, as well as NbC, remained constant in the investigated temperature range. For

determining the lattice parameters and weight fraction of the γ' phase, the synchrotron data were advantageous, as the isolated peaks, which were hardly visible in the conventional lab-source XRD data, were used. Interestingly, the γ-2 phase was observed in all lab-source diffractograms, but it was only found for the synchrotron measurements at temperatures close to 1000 °C.
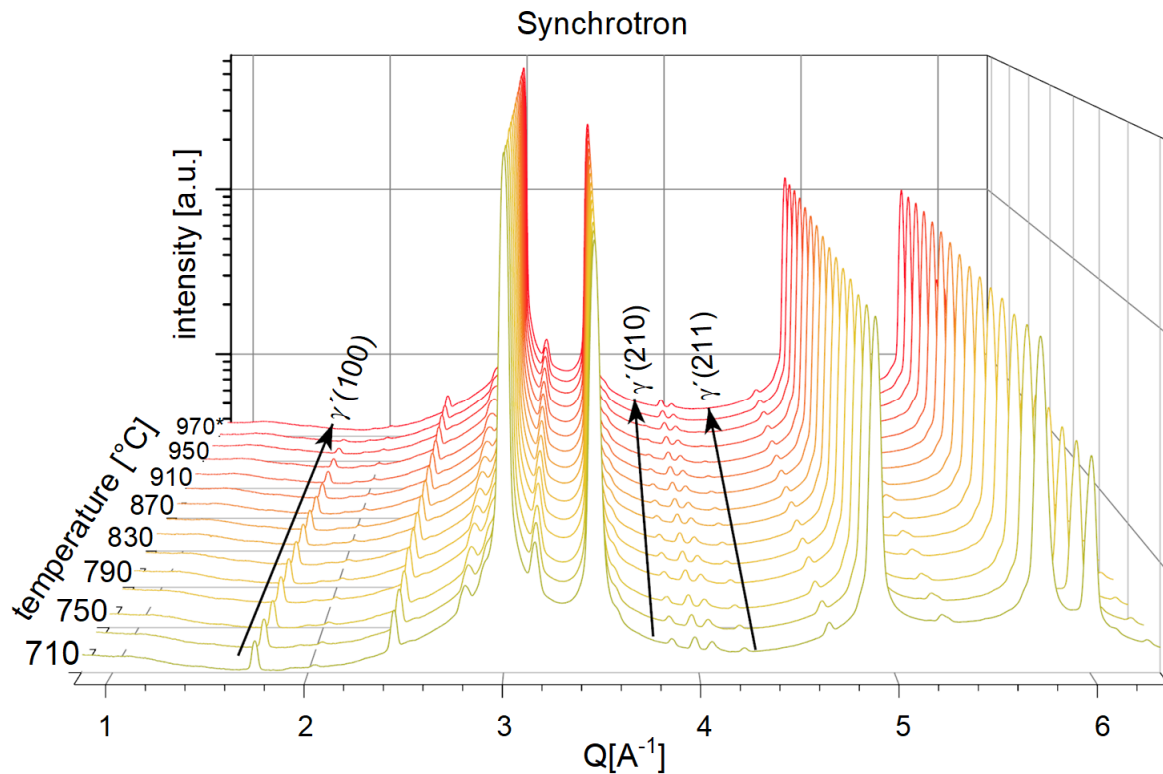

Figure 5. Synchrotron diffraction pattern of VDM Alloy 780 tested at different temperatures (710 °C to 970 °C).

In Figure 6, a detailed view of the Rietveld refinement of the (311) diffraction peaks (a) at the beginning (t = 1 min) and (b) at the end of the third holding segment (80 min) at 990° is depicted. The fraction of the γ-2 phase significantly increased at this temperature, from 20 wt.% to 57 wt.%. However, small amounts of the γ-2 phase were hard to detect in the case of the synchrotron measurements, due to the deep penetration depth of synchrotron radiation and the relatively low illuminated surface volume, in which the occurrence of the γ-2 phase was present. In addition, the fact that both phases, γ and γ-2, had the same crystal structure and only slightly different lattice constants and chemical compositions impeded the evaluation. The difference in the lattice parameter values of the synchrotron measurements between the γ (3.659 Å) and γ-2 (3.652 Å) phases was significantly smaller than that of the lab-source experiments. With our current knowledge, we cannot adequately explain the reason for the difference observed in the two methods. One possible explanation of this phenomenon will be discussed in Section 4.

An indicator for the emergence of the γ-2 phase was the introduction of a peak asymmetry into the previous symmetrical peak shape. During the first holding segment at 970 °C, the γ phase remained symmetric, while during holding at 980 °C, which can be regarded as the onset temperature for nucleation of the γ-2 phase, the first asymmetry increased.
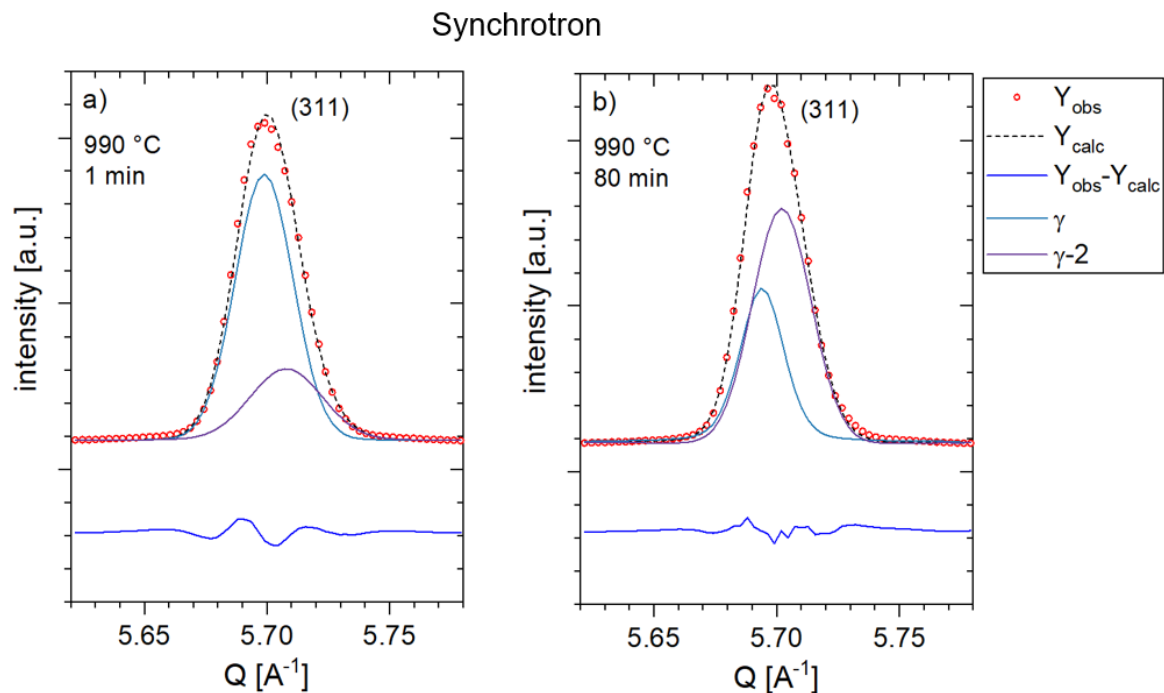
Synchrotron

Figure 6. Detailed view of Rietveld refinement (**a**) at the beginning (t = 1 min) and (**b**) at the end of the third holding segment (t = 80 min) at 990° of the (311) diffraction peaks: observed data (red circles), calculated data (black line), and difference plot (blue line). In these diffractograms, the simulated patterns of the γ and γ-2 phase are also shown.

The calculated lattice parameters of γ, γ', and γ-2 and the resulting lattice misfit between γ and γ' are depicted in Figure 7. In that figure, the γ matrix and the γ' hardening phase show a slightly larger lattice parameter for the lab-source experiments compared to those of the synchrotron XRD experiments. The development of the lattice parameter can be divided into different temperature segments. Tables 3 and 4 show the thermal expansion coefficient (TEC) of the phases in the different temperature ranges. The TEC was calculated by dividing the slope of the lattice parameter vs. temperature curves in the particular temperature segments by the lattice parameter at 25 °C.

Table 3. Linear thermal expansion coefficient of the different phases determined by lab-source XRD in the two temperature ranges.

	Lab Source		
	Linear Thermal Expansion Coefficient/10^{-6} [°C^{-1}]		
Temperature Range [°C]	γ	γ'	γ-2
25–800	14.4 ± 0.2	14.1 ± 0.1	17.8 ± 0.4
800–950	24.8 ± 1.0	19.1 ± 0.1	29.1 ± 0.6

The TEC of the γ-phase as determined via synchrotron and lab-source XRD agreed nicely up to 600 °C, as shown in the parallelism of the dashed blue curves in Figure 6. Similar behavior was also observed for the γ' phase, but with a slightly lower TEC for the synchrotron data, i.e., a lower slope of the trend line. The TEC of γ was slightly higher than that of γ', which resulted in a decreasing lattice misfit with increasing temperature. This phenomenon is well known for Ni-based superalloys [9–11].

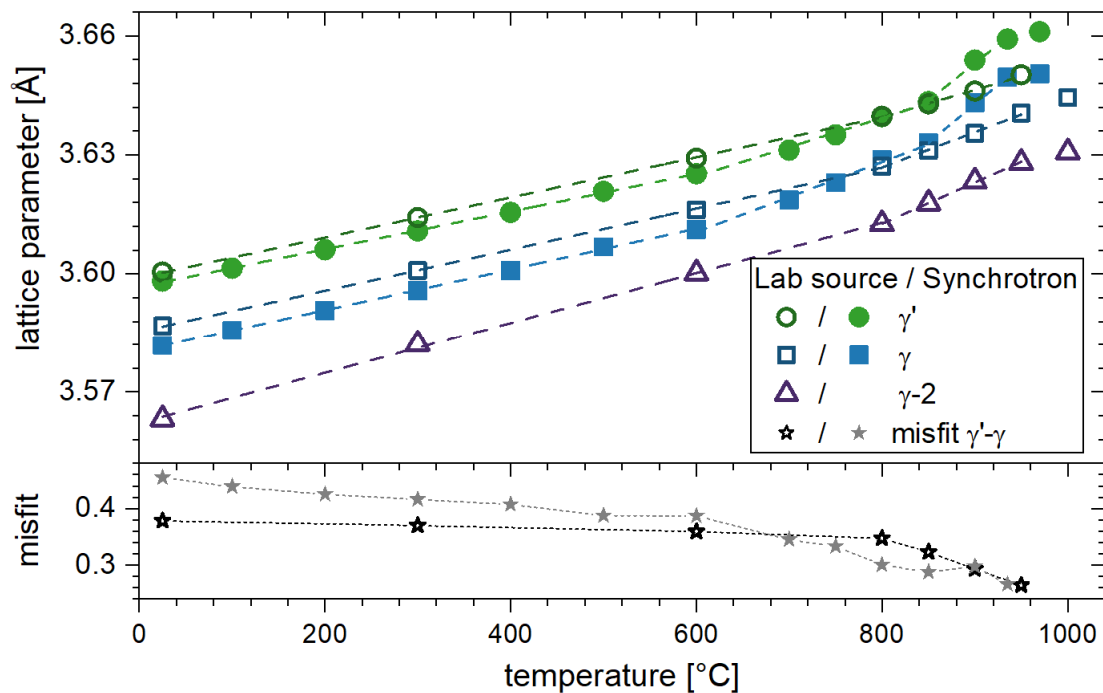**Figure 7.** Temperature-dependent lattice parameter and misfit of the γ', γ, and γ-2 phases, which were determined by X-ray and synchrotron diffraction. The synchrotron data are shown up to the first heating plateau of 970 °C.

Table 4. Linear thermal expansion coefficient of the different phases determined by synchrotron XRD in the three different temperature ranges.

	Synchrotron	
Temperature Range [°C]	**Linear Thermal Expansion Coefficient/10^{-6} [°C^{-1}]**	
	γ	γ'
25–600	14.4 ± 0.2	13.2 ± 0.1
600–850	24.6 ± 1.1	20.5 ± 1.0
850–935	54.4 ± 1.4	52.1 ± 0.4

In the synchrotron data starting from 600 °C, the increase in the lattice parameter of both phases was amplified, i.e., the TEC was enlarged. This increase was more pronounced in the γ phase, leading to an enhanced reduction of the lattice misfit. At temperatures exceeding 800 °C, the thermal expansion coefficient for the γ and γ' phases further increased. This effect will be discussed in more detail in Section 4. In the case of the lab-source XRD data, the onset of increased thermal expansion coefficients could not be determined with high precision, as no data from temperatures between 600 °C and 800 °C were measured.

The lattice parameter of the γ-2 phase developed in a manner similar to that of the γ phase in the whole temperature range, but with a slightly higher TEC. As a result, the lattice parameters of both phases converged with increasing temperature.

In Figure 8, the weight fraction of the γ' and γ-2 phases are depicted as a function of the temperature for both lab-source and synchrotron X-ray diffraction. The evolution of the γ' weight fraction with both techniques agreed nicely. The γ' weight fraction remained almost constant between 36 wt.% and 40 wt.%, up to 750 °C. At higher temperatures, the γ' weight fraction continuously decreased, and no γ' was measured at temperatures higher than 970 °C. The γ'-solvus temperature in this work was slightly lower when compared with previous ND results [25], in which a γ'-solvus temperature of approximately 995 °C to 1000 °C was determined. The weight fraction of the γ-2 phase increased continuously

from 800 °C upward in the lab-source X-ray measurements, and a maximum fraction of approximately 50% was reached at 1000 °C.
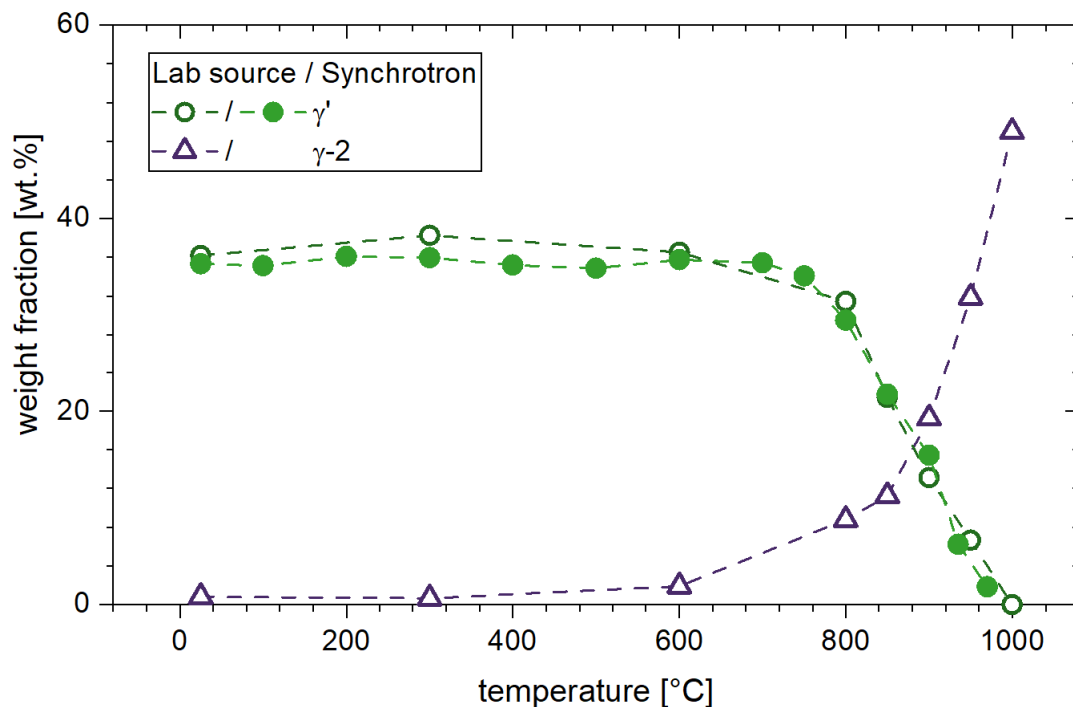

Figure 8. Temperature-dependent weight fractions of the γ' and γ-2 phases, which were determined by lab-source and synchrotron XRD. The synchrotron data are shown up to the first heating plateau of 970 °C.

The profile parameters of the γ and γ' phases and their evolution with temperature are shown in Figure 9a,b, respectively. The profile parameters of the LaB_6 reference measurements are also shown as a dashed baseline next to diagrams. Both strain and size were much more pronounced in the γ' phase than in the γ phase.

Both strain parameters (u and x) decreased almost linearly in the γ' phase in the temperature range from 25 °C to 800 °C. At higher temperatures, the decrease in both strain parameters was significantly steeper. This was related to the reducing lattice misfit between the γ and γ' phases. In addition, a notable peak broadening due to a small particle size was determined in the γ' phase. This size parameter remained constant up to a temperature of 600 °C and continuously increased at temperatures higher than 800 °C. These effects may be explained by the dissolution of γ', which began at 800 °C and reduced the γ' particle size.

The strain evolved in a non-linear manner in the γ phase. The strain parameter was almost constant at a rather small value up to a temperature of 600 °C. The strain noticeably increased at 800 °C, remained at this elevated level up to 900 °C and decreased at higher temperatures. No strain broadening was measured at 1000 °C. The increasing strain parameter between 600 °C and 800 °C may be explained by the beginning of the dissolution of the γ'-forming elements into the γ matrix. Concurrently, the above-mentioned decreasing lattice mismatch between the γ and γ' phases also reduced the strain in the γ phase. This effect and the decreasing fraction of the γ' phase led to a reduction of the strain parameters at higher temperatures. No peak broadening due to size effects were determined for the γ phase in most of the measured temperature range. The size parameter increased singly only at 1000 °C.
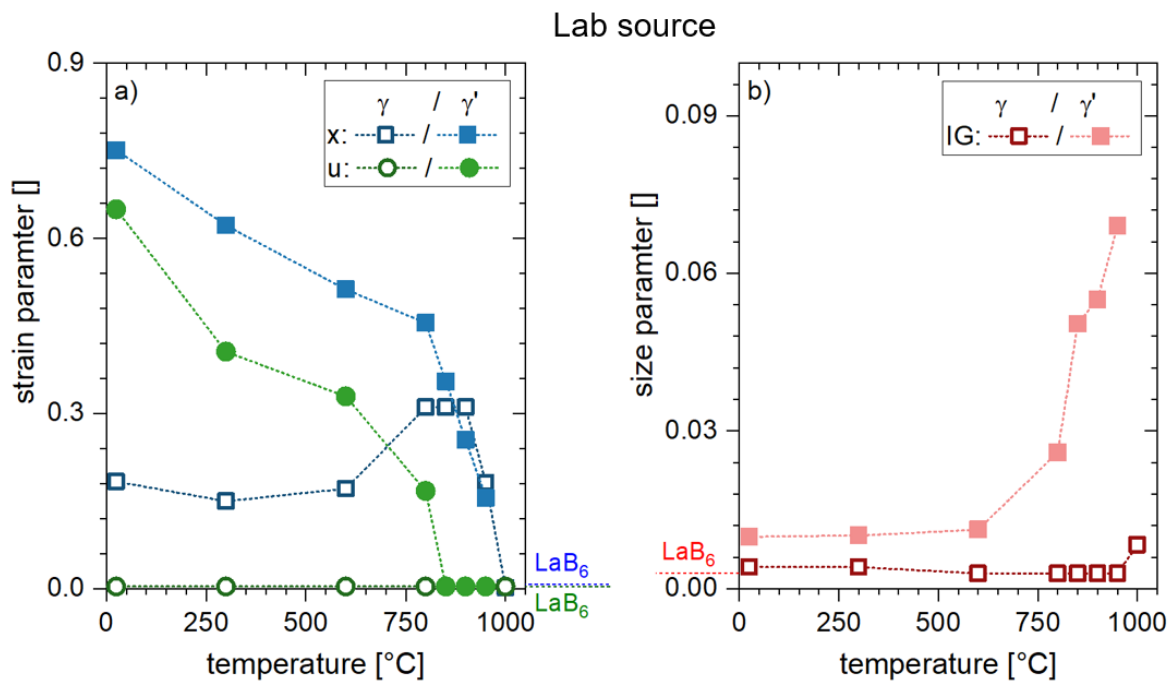
Figure 9. Evolution of (**a**) the strain parameter (u, x) and (**b**) the size parameter (IG) with rising testing temperature for the lab-source XRD experiments. The dashed lines next to the diagrams indicate the instrumental strain and size parameter, which were measured by LaB6. A higher strain or size parameter may be related to an increasing lattice strain or decreasing crystallite size, respectively.

3.3. Surface Oxidation Effects

Although all measurements were carried out in an inert gas atmosphere, the formation of oxides could not be excluded. Low Q-range diffraction patterns in the temperature ranged from 800 °C to 1000 °C for lab-source XRD and for holding segment at 990 °C, synchrotron XRD are shown in Figure 10a,b, respectively. In this Q-range, the evolution of different oxide phases (Al_2O_3 or Cr_2O_3) with increasing temperature were unambiguously visible. In the case of the lab-source diffraction experiments, the oxides started to grow at temperatures exceeding 800 °C. The oxide formation temperature was directly correlated to the formation temperature of the γ-2 phase. The maximum intensity of the oxide peaks in the lab-source XRD was only approximately one-seventh of that of the γ (111) peak. For the synchrotron measurements, the formation of oxide phases in the low Q range was observed in the second half of the holding segment at 980 °C by the onset of a peak asymmetry. However, the fraction strongly increased and a first quantification was only possible during the holding segment at 990 °C. Again, a direct correlation between the oxide formation and the formation of the γ-2 phase was visible.

To better understand the oxidation on the surface, two additional diffraction measurements were performed at room temperature with the lab source after the in-situ high temperature XRD. One measurement was performed directly after cooling down the sample (after previously heating the sample). For the second measurement, the surface was ground until a shiny metallic surface became visible and afterwards was polished to minimize the surface preparation effects. The XRD patterns of these conditions are shown in Figure 11. The initial sample condition (before heating) is also shown in Figure 11, for comparison. No Kβ-filter was used for these experiments. Therefore, additional peaks from the high scattering γ phase were visible at Q = 2.7 Å^{-1}, 3.1 Å^{-1}, 4.4 Å^{-1}, 5.2 Å^{-1}, and 5.4 Å^{-1}. The peaks from the oxides (Q = 1.5–2.5 Å^{-1}) were still visible after cooling down. However, these peaks diminished after the surface preparation. This was a clear indication that the oxidation peaks were only present close to the surface.
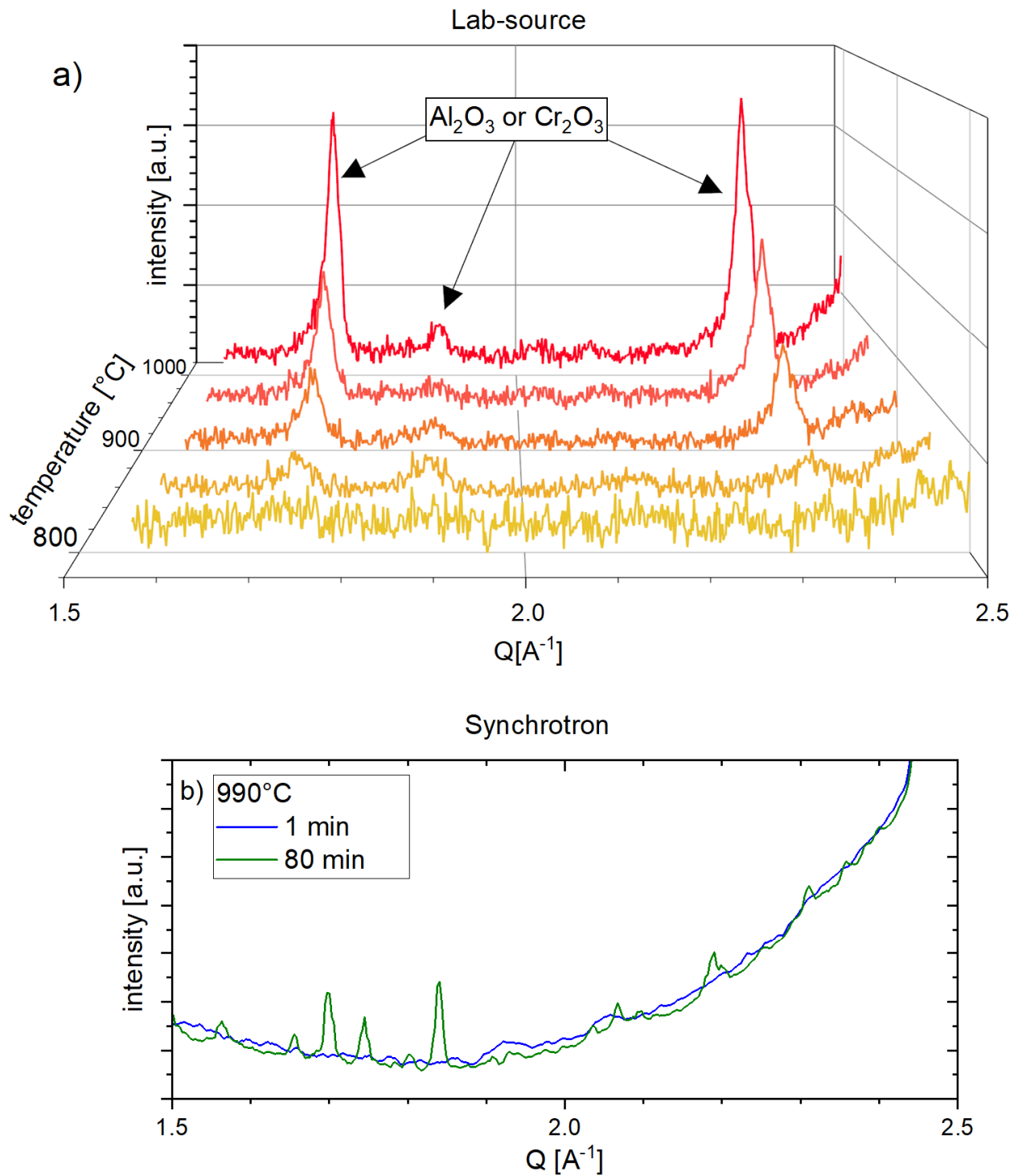
Figure 10. Low Q-range diffraction pattern showing the evolution of different oxide phases (Al_2O_3 or Cr_2O_3) measured during (**a**) lab-source and (**b**) synchrotron diffraction of VDM® Alloy 780 in the temperature range 800 °C to 1000 °C and for holding segment at 990 °C.
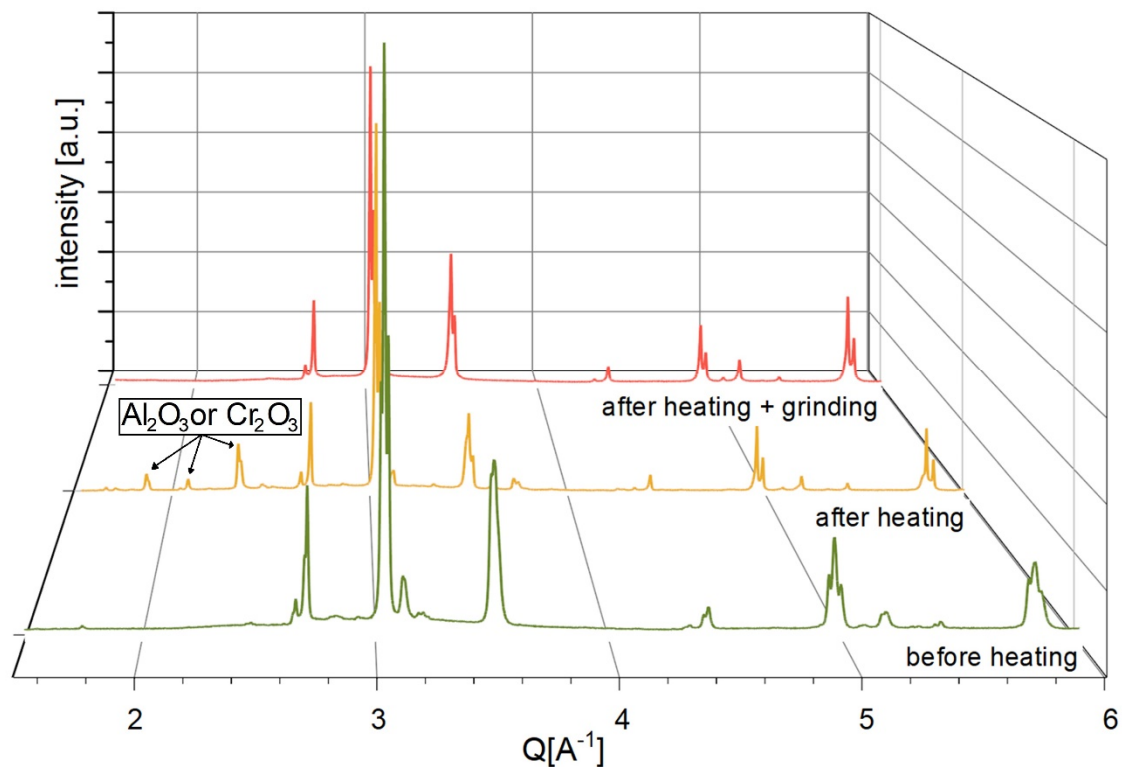
Figure 11. Diffraction patterns were taken at room temperature after different steps of the measuring program: (1) initial condition (before heating), (2) the condition after in-situ high-temperature XRD (after heating), (3) the condition after in-situ high-temperature XRD, surface grinding, and polishing (after heating + grinding).

4. Discussion

In this work, the dissolution behavior of the strengthening nano-sized γ'-hardening phase in the nickel-based high-temperature alloy VDM® Alloy 780 was investigated by in-situ lab-source and synchrotron XRD experiments in the temperature range from 25 °C to 1000 °C. The monitoring of all phases at high temperatures enabled us to understand the changes of the microstructure under such an external parameter. The two applied methods made it possible to compare the microstructure at the surface (lab source) with the bulk region (synchrotron). In the lab-source experiments, the samples were measured in reflection mode, and 99% of the X-rays were diffracted within the first 60 µm. In contrast, in the synchrotron measurements, samples with a diameter of 5 mm were measured in transmission mode, due to the much higher photon energy.

The lab-source XRD data were acquired during 95-min-long isothermal segments (15 min temperature stabilization followed by 80 min measurement). In contrast, the synchrotron data were acquired during continuous heating of the sample (due to the excellent statistics with the higher photon flux) at 10 °C/min up to a temperature of 970 °C. Starting from this temperature, three 80 min holding segments at 970 °C, 980 °C, and 990 °C were applied to study the time-dependent dissolution process of the γ' phase. The reason for this was the much faster acquisition of a diffraction pattern for synchrotron (4 s) compared with that of the lab-source (4800 s) experiments. Furthermore, it was not possible to repeat the long temperature steps of the lab-source experiments, due to the limited synchrotron measurement time.

The thermodynamic equilibrium was reached during the 15 min stabilization segment at the beginning of each temperature step in the lab source-experiments. The three individual X-ray diffraction patterns, which were recorded during one measuring segment, were very similar. This was also confirmed by a calculation of the mean distance of the

γ'-precipitates and the diffusion length of the dissolving γ'-forming elements Al and Nb within the Ni-matrix. Previous SANS measurements [26] showed that the mean size of the γ'-precipitates is 35 nm in VDM® Alloy 780 in its as-received condition. Assuming round γ'-precipitates, this led to a minimum distance of only 4 nm between two γ' precipitates at a γ' volume fraction of 35%. The diffusion of Al and Nb was calculated by an Arrhenius equation and literature data for the diffusion from Al and Nb in Ni ($D_{0,\,Al}$ = 1.1 cm^2/s and E_{Al} = 249 kJ/mol [40], $D_{0,\,Nb}$ = 0.1618 cm^2/s and E_{Nb} = 234 kJ/mol [41], where D_0 is the maximal diffusion coefficient and E is the activation energy for diffusion). In Figure 12, the diffusion rates of Al and Nb in Ni are shown in the testing temperature on a logarithmic scale. The diffusion rate was very similar for Al and Nb and increased from 0.5 nm/s$^{1/2}$ (Al) or 0.5 nm/s$^{1/2}$ (Nb) at 600 °C to 115 nm/s$^{1/2}$ (Al) or 90 nm/s$^{1/2}$ at 1000 °C. The diffusion length of Al and Nb exceeded the γ'-$\gamma\gamma'$ distance, starting from 600 °C for both elements during the initial 15 min stabilization segment (17 nm for Nb and 16 nm for Al).
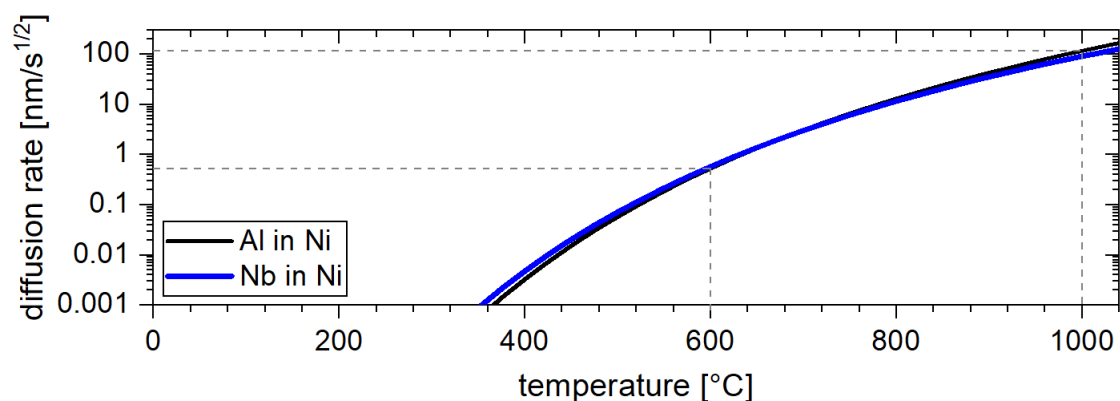

Figure 12. Calculated diffusion rate for aluminum and niobium in nickel. The diffusion rate was calculated by an Arrhenius equation and literature data for Al [40] and Nb [41] in Ni.

Despite these experimental differences between the lab-source and synchrotron X-ray diffraction experiments, the γ' dissolution process was very similar for both methods and was subdivided into different temperature regions:

- The weight fraction and size of the γ' phase remained nearly constant from room temperature until approximately 750 °C in the surface and bulk regions of the sample. This temperature range was characterized by a linear reduction in the lattice misfit between γ' and γ, due to the higher thermal expansion coefficient of the matrix. As a result, the strain in the γ' phase continuously decreased with increasing temperature. This linear reduction in the lattice misfit in the temperature range from 25 °C to 750 °C is known for a variety of Ni-based superalloys; see, e.g., references [9–11].
- The phase fraction of γ' rapidly decreased at higher temperatures (800–970 °C). No γ' was measured at temperatures exceeding 970 °C. The decreasing fraction of γ' was accompanied by an increasing size-broadening parameter of the γ' peaks, which indicated a decreasing crystallite size. Furthermore, the lattice misfit and strain significantly reduced in this temperature range.

The development of the lattice parameters during the dissolution of γ' was dependent on two mechanisms:

- The dissolution of the γ'-forming elements Al and Nb into the γ matrix led to an increasing γ lattice parameter. This may be better explained by the significantly higher atomic radii of the γ'-forming elements Al and Nb (1.432 Å and 1.47 Å) [42] than by the atomic radii of γ forming elements Ni, Co and Cr (1.246 Å, 1.253 Å and 1.29 Å) [42]. Previous ND results [25] revealed that a decreasing amount of γ' leads to an increasing γ lattice parameter.

- Surface oxidation occurs at temperatures higher than 800 °C. It is well known from the relevant literature that the thickness of the oxide layer strongly depends on the testing temperature, time, and atmosphere. The oxides in Ni-based superalloys preferably bind Al, Cr, Fe, Mo and Nb [43,44]. According to the literature, an oxide layer thickness of a few nanometers when tested at room temperature [44], increases to a thickness of tens of micrometers when tested at 750 °C [45].As a result of the oxidation, a chemically modified γ phase (γ-2) developed in the sub-surface area, which was enriched in Ni and depleted in the oxide-forming elements [44]. This rich γ-2 layer was much thicker than the oxide layer, due to the high diffusibility of the oxide-forming elements.

It may be assumed that the oxidation in the lab-source experiments was more pronounced than it was in the synchrotron experiments due to the longer time exposure. The oxide phases could be directly measured with the surface sensitive lab source at temperatures of 800 °C and above. In contrast, the development of the oxidation phase was only marginally measurable in the synchrotron experiments. Small diffraction peaks of the oxide phases were detectable in the synchrotron only after long exposure times at 990 °C, due to the relatively small thickness of the oxide layer in relation to the total measured thickness of the sample. The oxidation influenced the development of the γ lattice parameter. The thermal expansion coefficient of the γ phase was much smaller at the surface than in the bulk region of the sample at temperatures higher than 850 °C. The larger Al and Nb atoms, which originated from the dissolving γ' precipitates, initially dissolved fully within the γ-matrix. However, these elements diffused to the surface to build oxides. The mean diffusion path for Al/Nb was about 180/120 μm with a holding time of 95 min at 950 °C, which was significantly higher than the mean penetration depth of the X-rays in the lab-source experiments.

Due to the oxidation in the surface region, a γ-2 phase was formed. The γ-2 phase was characterized by a smaller lattice parameter compared to that of the initial γ phase (which was closer to the lattice parameter of pure Ni). The lab-source X-ray diffraction experiments were very surface-sensitive due to the low energy of X-rays, resulting in a low penetration depth in these experiments. Therefore, the γ-2 phase was detectable in all lab-source XRD measurements, even at room temperature, where the thickness of the oxide layer was only in the low nm regime [44]. The fraction of the γ-2 phase was stable at a relatively low value (<2 wt.%) at temperatures up to 600 °C. The fraction of the γ-2 phase and, therefore, the fraction of oxides, significantly increased in the same temperature range (800 °C to 1000 °C), as the dissolution of the γ' phase was due to the long holding segments in these experiments. The composition of this new phase obviously changed after dissolution of the γ' phase, as the thermal expansion coefficient noticeably increased above 800 °C. The γ-2 phase began to develop clearly during the holding segments at very high temperatures (T = 990 °C), after the γ' phase was dissolved in the synchrotron experiments, as the growth of oxide was a time-consuming process. Furthermore, the lattice parameter of the γ-2 phase was smaller in the synchrotron experiments, compared with the one in the lab-source experiments. The most plausible explanation of this phenomenon is that there was a higher amount of Al and Nb in the γ-2 phase in the synchrotron experiments, due to reduced oxidation in these tests.

Whether the γ-2 phase influences mechanical properties at the surface will be the subject of future investigations. On the one hand, the lattice misfit between γ-2 and γ' (0.69% at 850 °C) was considerably higher than the misfit between the original γ and γ' (0.32% at 850 °C). As a result, the strengthening mechanism of the γ' phase was higher in the γ-2 phase. This effect was of particular interest in the temperature range from 800 °C to 900 °C because of the simultaneous presence of a high fraction of γ-2 (between 9 and 19 wt.%) and γ' (between 31 and 13 wt.%) at the surface. On the other hand, the solution of Al and Nb strengthened the matrix phase. This effect was less pronounced in the γ-2 phase compared to the γ phase.

5. Conclusions

The paper underpins how the combination of in-situ high-temperature lab-source and synchrotron diffraction is suitable for analyzing the lattice parameters and volume fractions of the phases that are typically present in polycrystalline Ni-based superalloys in the near-surface and bulk regions. The maximum penetration depth of the X-rays was approximately 60 μm in the lab source. In contrast, samples with a diameter of 5 mm were measured in transmission mode in the synchrotron measurements. The major findings of this study are as follows:

- The dissolution behavior of the strengthening γ' phase with increasing temperatures was nearly identical in the surface and bulk regions in the investigated VDM® Alloy 780. The γ' weight fraction and size remained nearly constant until a temperature of approximately 750 °C was reached. The γ'-phase fraction rapidly decreased at higher temperatures and no γ' was measured at temperatures exceeding 970 °C.
- The dissolution of the larger γ'-forming elements, Al and Nb, into the γ matrix led to an increasing γ lattice parameter. However, the extent significantly differed at the surface or in the bulk of the sample. This may be explained by the surface oxidation effects at temperatures exceeding 800 °C.
- The increase of the γ lattice parameters was much higher in the bulk region compared to the surface region. The larger Al and Nb atoms, which originated from the dissolving γ' precipitates, fully dissolved within the γ-matrix in the bulk region.
- These elements diffused to the surface to build oxides in the sub-surface area. As a result, a chemically modified γ phase (γ-2) with a smaller lattice parameter as its parental γ phase developed.
- The results showed that the investigated VDM® Alloy 780 is a suitable candidate for highly stressed parts in the hot sections of modern gas turbine engines and power generation applications, where temperatures of up to 750 °C are targeted. The γ' fraction remained stable at high temperature values up to 800 °C.

References

1. Pollock, T.M.; Argon, A.S. Creep resistance of CMSX-3 nickel base superalloy single crystals. *Acta Metall. Mater.* **1992**, *40*, 1–30. [CrossRef]
2. Chen, J.H.; Rogers, P.M.; Little, J.A. Oxidation behaviour of several chromia-forming commercial nickel-base superalloys. *Oxid. Met.* **1997**, *47*, 381–410. [CrossRef]
3. Murakumo, T.; Kobayashi, T.; Koizumi, Y.; Harada, H. Creep behaviour of Ni-base single-crystal superalloys with various γ' volume fraction. *Acta Mater.* **2004**, *52*, 3737–3744. [CrossRef]
4. Pineau, A.; Antolovich, S.D. High temperature fatigue of nickel-base superalloys—A review with special emphasis on deformation modes and oxidation. *Eng. Fail. Anal.* **2009**, *16*, 2668–2697. [CrossRef]

5. Li, J.; Wahi, R.P. Investigation of γ/γ' lattice mismatch in the polycrystalline nickel-base superalloy IN738LC: Influence of heat treatment and creep deformation. *Acta Metall. Mater.* **1995**, *43*, 507–517. [CrossRef]

6. Soula, A.; Renollet, Y.; Boivin, D.; Pouchou, J.-L.; Locq, D.; Caron, P.; Bréchet, Y. Analysis of high-temperature creep deformation in a polycrystalline nickel-base superalloy. *Mater. Sci. Eng. A* **2009**, *510–511*, 301–306. [CrossRef]

7. Cozar, R.; Pineau, A. Morphology of y' and y'' precipitates and thermal stability of inconel 718 type alloys. *Metall. Trans.* **1973**, *4*, 47–59. [CrossRef]

8. Kotval, P.S. The microstructure of superalloys. *Metallography* **1969**, *1*, 251–285. [CrossRef]

9. Grose, D.A.; Ansell, G.S. The influence of coherency strain on the elevated temperature tensile behaviour of Ni-15Cr-AI-Ti-Mo alloys. *Metall. Trans. A* **1981**, *12*, 1631–1645. [CrossRef]

10. Nathal, M.V.; Mackay, R.A.; Garlick, R.G. Temperature dependence of γ-γ' lattice mismatch in Nickel-base superalloys. *Mater. Sci. Eng.* **1985**, *75*, 195–205. [CrossRef]

11. Kamara, A.B.; Ardell, A.J.; Wagner, C.N.J. Lattice misfits in four binary Ni-Base $\gamma/\gamma 1$ alloys at ambient and elevated temperatures. *Metall. Mater. Trans. A* **1996**, *27*, 2888–2896. [CrossRef]

12. Collier, J.P.; Selius, A.O.; Tien, J.K. On developing a microstructurally and thermally stable iron-nickel base superalloy. *Superalloys* **1988**, *1988*, 43–52.

13. Zenk, C.H.; Neumeier, S.; Stone, H.J.; Göken, M. Mechanical properties and lattice misfit of γ/γ' strengthened Co-base superalloys in the Co–W–Al–Ti quaternary system. *Intermetallics* **2014**, *55*, 28–39. [CrossRef]

14. Gao, S.; Hou, J.; Yang, F.; Guo, Y.; Zhou, L. Effect of Ta on microstructural evolution and mechanical properties of a solid-solution strengthening cast Ni-based alloy during long-term thermal exposure at 700 °C. *J. Alloys Compd.* **2017**, *729*, 903–913. [CrossRef]

15. Azadian, S.; Wei, L.-Y.; Warren, R. Delta phase precipitation in Inconel 718. *Mater. Charact.* **2004**, *53*, 7–16. [CrossRef]

16. Messé, O.M.; Barnard, J.S.; Pickering, E.J.; Midgley, P.A.; Rae, C.M.F. On the precipitation of delta phase in ALLVAC® 718Plus. *Philos. Mag.* **2014**, *94*, 1132–1152. [CrossRef]

17. Mitchell, A. Primary Carbides in Alloy 718. In Proceedings of the 7th International Symposium on Superalloy 718 and Derivatives, Pittsburgh, PA, USA, 10–13 October 2012; pp. 161–167.

18. Oblak, J.M.; Paulonis, D.F.; Duvall, D.S. Coherency strengthening in Ni base alloys hardened by DO22 γ' precipitates. *Metall. Trans.* **1974**, *5*, 143–153. [CrossRef]

19. Sundararaman, M.; Mukhopadhyay, P.; Banerjee, S. Precipitation of the δ-Ni3Nb phase in two nickel base superalloys. *Metall. Trans. A* **1988**, *19*, 453–465. [CrossRef]

20. Cao, W.-D.; Kennedy, R. Role of chemistry in 718-type alloys—Allvac® 718plus™ alloy development. *Superalloys* **2004**, *2004*, 91–99.

21. Kirchmayer, A.; Lyu, H.; Pröbstle, M.; Houllé, F.; Förner, A.; Huenert, D.; Göken, M.; Felfer, P.J.; Bitzek, E.; Neumeier, S. Combining Experiments and Atom Probe Tomography-Informed Simulations on γ' Precipitation Strengthening in the Polycrystalline Ni-Base Superalloy A718Plus. *Adv. Eng. Mater.* **2020**, *22*, 2000149. [CrossRef]

22. Neumeier, S.; Freund, L.P.; Göken, M. Novel wrought γ/γ' cobalt base superalloys with high strength and improved oxidation resistance. *Scr. Mater.* **2015**, *109*, 104–107. [CrossRef]

23. Bergner, M.; Rösler, J.; Gehrmann, B.; Klöwer, J. Effect of Heat Treatment on Microstructure and Mechanical Properties of VDM Alloy 780 Premium. In *Proceedings of the 9th International Symposium on Superalloy 718 & Derivatives: Energy, Aerospace, and Industrial Applications*; Ott, E., Liu, X., Andersson, J., Bi, Z., Bockenstedt, K., Dempster, I., Groh, J., Heck, K., Jablonski, P., Kaplan, M., et al., Eds.; Springer International Publishing: Cham, Switzerland, 2018; pp. 489–499.

24. Rösler, J.; Hentrich, T.; Gehrmann, B. On the Development Concept for a New 718-Type Superalloy with Improved Temperature Capability. *Metals* **2019**, *9*, 1130. [CrossRef]

25. Solís, C.; Munke, J.; Bergner, M.; Kriele, A.; Mühlbauer, M.J.; Cheptiakov, D.V.; Gehrmann, B.; Rösler, J.; Gilles, R. In Situ Characterization at Elevated Temperatures of a New Ni-Based Superalloy VDM-780 Premium. *Metall. Mater. Trans. A Phys. Metall. Mater. Sci.* **2018**, *49*, 4373–4381. [CrossRef]

26. Solís, C.; Munke, J.; Hofmann, M.; Mühlbauer, S.; Bergner, M.; Gehrmann, B.; Rösler, J.; Gilles, R. In situ characterization at high temperature of VDM Alloy 780 premium to determine solvus temperatures and phase transformations using neutron diffraction and small-angle neutron scattering. In *Characterization of Minerals, Metals, and Materials 2019*; Minerals, Metals and Materials Series; Springer: Cham, Switzerland, 2019; pp. 23–32.

27. Ghica, C.; Solís, C.; Munke, J.; Stark, A.; Gehrmann, B.; Bergner, M.; Rösler, J.; Gilles, R. HRTEM analysis of the high-temperature phases of the newly developed high-temperature Ni-base superalloy VDM 780 Premium. *J. Alloys Compd.* **2020**, *814*, 152–157. [CrossRef]

28. Kümmel, F.; Kirchmayer, A.; Solís, C.; Hofmann, M.; Neumeier, S.; Gilles, R. Deformation Mechanisms in Ni-Based Superalloys at Room and Elevated Temperatures Studied by In Situ Neutron Diffraction and Electron Microscopy. *Metals* **2021**, *11*, 719. [CrossRef]

29. Gilles, R.; Mukherji, D.; del Genovese, D.; Strunz, P.; Barbier, B.; Kockelmann, W.; Rösler, J.; Fuess, H. Misfit investigations of Nickel-base superalloys. *Mater. Sci. Forum* **2003**, *426–432*, 821–826.

30. Mukherji, D.; Gilles, R.; Barbier, B.; Genovese, D.D.; Hasse, B.; Strunz, P.; Wroblewski, T.; Fuess, H.; Rösler, J. Lattice misfit measurement in Inconel 706 containing coherent γ' and γ'' precipitates. *Scr. Mater.* **2003**, *48*, 333–339. [CrossRef]

31. Schell, N.; King, A.; Beckmann, F.; Fischer, T.; Müller, M.; Schreyer, A. The High Energy Materials Science Beamline (HEMS) at PETRA III. *Mater. Sci. Forum* **2014**, *772*, 57–61.

32. Hammersley, A.P. FIT2D: An Introduction and Overview, ESRF Internal Report ESRF97HA02T (1997). Available online: https://www.esrf.fr/computing/scientific/FIT2D/FIT2D_INTRO/fit2d.html (accessed on 15 January 2022).

33. Rodríguez-Carvajal, J. Recent advances in magnetic structure determination by neutron powder diffraction. *Phys. B* **1993**, *192*, 55–69. [CrossRef]

34. Thompson, P.; Cox, D.E.; Hastings, J.B. Rietveld refinement of Debye–Scherrer synchrotron X-ray data from Al2O3. *J. Appl. Crystallogr.* **1987**, *20*, 79–83. [CrossRef]

35. Solís, C.; Kirchmayer, A.; Silva, I.d.; Kümmel, F.; Mühlbauer, S.; Beran, P.; Gehrmann, B.; Haghighat, M.H.; Neumeier, S.; Gilles, R. Monitoring the precipitation of the hardening phase in the new VDM® Alloy 780 by insitu high-temperature small-angle neutron scattering, neutron diffraction and complementary microscopy techniques. *J. Alloys Compd.* **2022**, accepted.

36. Hwang, J.-W. Thermal Expansion of Nickel and Iron, and the Influence of Nitrogen on the Lattice Parameter of Iron at the Curie Temperature. Master's Thesis, University of Missouri, Columbia, MI, USA, 1972.

37. Gilles, R.; Krimmer, B.; Boysen, H.; Fuess, H. Status of the new structure powder diffractometer (SPODI) at the FRM-II in Garching. *Appl. Phys. A* **2002**, *74*, s148–s150. [CrossRef]

38. Hoelzel, M.; Senyshyn, A.; Juenke, N.; Boysen, H.; Schmahl, W.; Fuess, H. High-resolution neutron powder diffractometer SPODI at research reactor FRM II. Nucl. Instrum. *Methods Phys. Res. Sect. A* **2012**, *667*, 32–37.

39. Hoelzel, M.; Senyshyn, A.; Dolotko, O. SPODI: High resolution powder diffractometer. *J. Large-Scale Res. Facil. JLSRF* **2015**, *1*, 5. [CrossRef]

40. Allison, H.W.; Samelson, H. Diffusion of Aluminum, Magnesium, Silicon, and Zirconium in Nickel. *J. Appl. Phys.* **1959**, *30*, 1419–1424. [CrossRef]

41. Sohrabi, M.J.; Mirzadeh, H. Revisiting the Diffusion of Niobium in an As-Cast Nickel-Based Superalloy During Annealing at Elevated Temperatures. *Met. Mater. Int.* **2020**, *26*, 326–332. [CrossRef]

42. Wiberg, E.; Wiberg, N. *Hollemann-Wiberg, Lehrbuch der Anorganischen Chemie, 101*; Walter de Gruyter & Co.: Berlin, Germany; New York, NY, USA, 1995.

43. Nowak, W.J. Characterization of oxidized Ni-based superalloys by GD-OES. *J. Anal. At. Spectrom.* **2017**, *32*, 1730–1738. [CrossRef]

44. Larsson, A.; D'Acunto, G.; Vorobyova, M.; Abbondanza, G.; Lienert, U.; Hegedüs, Z.; Preobrajenski, A.; Merte, L.R.; Eidhagen, J.; Delblanc, A.; et al. Thickness and composition of native oxides and near-surface regions of Ni superalloys. *J. Alloys Compd.* **2022**, *895*, 162657. [CrossRef]

45. Cruchley, S.; Evans, H.; Taylor, M. An overview of the oxidation of Ni-based superalloys for turbine disc applications: Surface condition, applied load and mechanical performance. *Mater. High Tep.* **2016**, *33*, 465–475. [CrossRef]